The Astrophysical Journal Letters, 992:L10 (13pp), 2025 October 10 https://doi.org/10.3847/2041-8213/ae04de
© 2025. The Author(s). Published by the American Astronomical Society.
OPEN ACCESS

The Type II SN 2025pht in NGC 1637: A Red Supergiant with Carbon-rich Circumstellar Dust as the First JWST Detection of a Supernova Progenitor Star

Charles D. Kilpatrick[1], Aswin Suresh[1,2], Kyle W. Davis[3], Maria R. Drout[4], Ryan J. Foley[3], Alexander Gagliano[5,6,7], Wynn V. Jacobson-Galán[8,10], Ravjit Kaur[3], Kirsty Taggart[3], and Jason Vazquez[9]
[1] Center for Interdisciplinary Exploration and Research in Astrophysics (CIERA), Northwestern University, Evanston, IL 60201, USA; ckilpatrick@northwestern.edu
[2] Department of Physics and Astronomy, Northwestern University, Evanston, IL 60201, USA
[3] Department of Astronomy and Astrophysics, University of California, Santa Cruz, CA 95064, USA
[4] David A. Dunlap Department of Astronomy and Astrophysics, University of Toronto, 50 St George Street, Toronto, ON M5S 3H4, Canada
[5] The NSF Institute for Artificial Intelligence and Fundamental Interactions, USA
[6] Center for Astrophysics | Harvard & Smithsonian, Cambridge, MA 02138, USA
[7] Department of Physics and Kavli Institute for Astrophysics and Space Research, Massachusetts Institute of Technology, 77 Massachusetts Avenue, Cambridge, MA 02139, USA
[8] Cahill Center for Astrophysics, California Institute of Technology, MC 249-17, 1216 E. California Boulevard, Pasadena, CA 91125, USA
[9] Department of Physics, University of Wisconsin–Milwaukee, 3135 North Maryland Avenue, Milwaukee, WI 53211, USA
Received 2025 August 14; revised 2025 September 5; accepted 2025 September 7; published 2025 October 8

Abstract

We present follow-up imaging and spectroscopy and pre-explosion imaging of SN 2025pht located in NGC 1637 at 12 Mpc. Our spectroscopy shows that SN 2025pht is a Type II supernova (SN) with broad lines of hydrogen and with minimal line-of-sight extinction inferred from Na I D absorption. NGC 1637 was the target of several epochs of Hubble Space Telescope (HST) and James Webb Space Telescope (JWST) imaging covering the site of SN 2025pht from 31 to 0.7 yr prior to discovery. Using a follow-up HST image of SN 2025pht aligned to these data, we demonstrate that there is a credible progenitor candidate detected in multiple epochs of HST imaging and in JWST imaging from 1.3 to 8.7 μm, the first JWST counterpart to an SN and the longest-wavelength detection of an SN progenitor star. Fitting this source to red supergiant (RSG) spectral energy distributions (SEDs), we show that it is consistent with a $\log(L/L_{\odot}) = 5.0$ RSG heavily reddened by circumstellar dust. The JWST photometry enables strong constraints on the nature of the circumstellar medium, and we find that the SED favors graphite-rich dust as opposed to silicate-rich dust and an optical circumstellar extinction of $A_V = 5.3$ mag. We discuss the implications of a pre-SN RSG enshrouded in carbon-rich dust and this finding for the overall population of progenitor stars to Type II SNe, as well as the future of SN progenitor star discovery with JWST.

Unified Astronomy Thesaurus concepts: Type II supernovae (1731); Massive stars (732)

Materials only available in the online version of record: data behind figure,

1. Introduction

Since the discovery of the blue supergiant progenitor star Sanduleak −69 202 to SN 1987A (R. P. Kirshner et al. 1987; R. M. West et al. 1987; S. E. Woosley et al. 1987; W. D. Arnett et al. 1989), over 30 other progenitor stars to core-collapse supernovae (SNe) have been identified in pre-explosion imaging (e.g., S. J. Smartt 2009; S. D. Van Dyk et al. 2012, 2023a; J. R. Maund et al. 2013; L. Tomasella et al. 2013; M. Fraser et al. 2014; C. D. Kilpatrick & R. J. Foley 2018; D. O'Neill et al. 2019; J. Sollerman et al. 2021; C. D. Kilpatrick et al. 2023b, 2023a; D. Xiang et al. 2024). The vast majority of these systems are red supergiant (RSG) progenitor stars to Type II SNe (SNe II; see reviews in, e.g., S. J. Smartt 2015; S. D. Van Dyk 2017), the predicted terminal state for single stars with initial masses ≈8–30 $M_{\odot}$ (corresponding to RSGs with terminal luminosities of $\log(L/L_{\odot}) \approx 4.3$–5.6 at solar metallicities; see, e.g., B. Davies et al. 2013; J. Choi et al. 2016). Despite the robust detections of several RSGs discovered as progenitor stars to SNe II and with inferred luminosities from $\log(L/L_{\odot}) = 4.3$ to 5.2, no sources have been claimed with luminosities exceeding this range.

The mismatch between the luminosities of the observed population of SN II progenitor stars and the overall field population of RSGs led to claims that there are "missing" high-mass SN progenitor stars (the "red supergiant problem"; S. J. Smartt 2015). Although this phenomenon could arise at random owing to the limited number of SN II progenitor stars (B. Davies & E. R. Beasor 2020a; but see also C. S. Kochanek 2020; B. Davies & E. R. Beasor 2020b), our limited understanding of late-stage RSG evolution and thus the true spectral shape of these stars (J. J. Walmswell & J. J. Eldridge 2012; B. Davies & B. Plez 2021; B. Davies et al. 2022), the increasing incidence of close binary interactions among high-mass stars and their evolution into the progenitors of stripped-envelope SNe (N. Smith et al. 2011; E. Zapartas et al. 2021), or some combination of the above, there are theoretical expectations and observational evidence that some $\log(L/L_{\odot}) = 5.2$–5.6 RSGs do not explode as SNe. These stars tend to have highly compact oxygen cores (T. Ertl et al. 2016; T. Sukhbold et al. 2016), which disfavor successful SN explosions and suggest that they may instead collapse directly into black holes with at most a weak explosion (E. O'Connor & C. D. Ott 2011; A. L. Piro 2013; R. Fernández et al. 2018).

[10] NASA Hubble Fellow.

Original content from this work may be used under the terms of the Creative Commons Attribution 4.0 licence. Any further distribution of this work must maintain attribution to the author(s) and the title of the work, journal citation and DOI.

This phenomenon was invoked to explain a "disappearing" 25 $M_\odot$ RSG in NGC 6946 (S. M. Adams et al. 2017) and more recently a 20 $M_\odot$ RSG in M31 (K. De et al. 2024). Systematic searches for these disappearing stars can place upper limits on the fraction of RSGs that produce these "failed" SNe (C. S. Kochanek 2014; E. J. Farrell et al. 2020; R. A. Byrne & M. Fraser 2022), while the population of RSGs observed as SN II progenitor stars can explain the remainder of the terminal RSG population.

However, the impact of circumstellar extinction on direct imaging of SN progenitor stars is difficult to quantify owing to the lack of deep, multiband infrared (IR) imaging. A limited number of SN II progenitor stars are detected in ground-based IR, Hubble Space Telescope (HST) Near Infrared Camera and Multi-Object Spectrometer (NICMOS) or Wide Field Camera 3 (WFC3) IR, or Spitzer Infrared Array Camera (IRAC) images (e.g., SN 2005cs, SN 2012aw, SN 2017eaw, SN 2022acko, SN 2023ixf, and SN 2024ggi; W. Li et al. 2006; C. S. Kochanek et al. 2012; C. D. Kilpatrick & R. J. Foley 2018; C. D. Kilpatrick et al. 2023b; S. D. Van Dyk et al. 2023a; D. Xiang et al. 2024). In modeling the spectral energy distributions (SEDs) of some of these sources, they appear significantly cooler than expectations for a bare RSG photosphere. Even accounting for expectations that RSGs evolve toward later spectroscopic types as they approach SNe (B. Davies & E. R. Beasor 2018), standard RSG models cannot accurately describe several sources with blackbody temperatures significantly cooler than 3000 K. Their SEDs imply the presence of a photosphere at radii significantly larger than even the most extreme RSGs (i.e., larger than 2000 $R_\odot$ as in B. Davies et al. 2007) and thus the existence of a dense, optically thick shell of circumstellar material (CSM). The composition of these shells produced at such late evolutionary phases, the mass-loss rates they imply from the progenitor star, and the total circumstellar extinction they impart on the underlying star can be partly constrained from early-time light curves and "flash spectroscopy" of SNe (A. Gal-Yam et al. 2014; D. Khazov et al. 2016; W. V. Jacobson-Galán et al. 2024), but the connection to progenitor stars is only now being studied via exceptional events such as SN 2023ixf (J. E. Jencson et al. 2023; C. D. Kilpatrick et al. 2023a; Z. Niu et al. 2023; J. L. Pledger & M. M. Shara 2023; M. D. Soraisam et al. 2023; J. M. M. Neustadt et al. 2024; S. D. Van Dyk et al. 2024).

Detailed SED modeling of the SN 2023ixf progenitor star implies a total optical extinction of as much as $A_V \approx 5$ mag toward the underlying star (C. D. Kilpatrick et al. 2023a), significantly in excess of previous treatment of circumstellar extinction from normal RSG winds where even the highest mass-loss rates were assumed to yield dense CSM with line-of-sight extinction of $A_V < 1$ mag (as in J. J. Walmswell & J. J. Eldridge 2012). However, IR detections of nearby counterparts to other SNe, where emission from the star is reprocessed through these optically thick shells of CSM, are needed to better constrain the total amount of light from the star. With detections at longer mid-IR wavelengths, the composition of this material can also be constrained from broadband silicate and polycyclic aromatic hydrocarbon emission similar to those observed in the spectra of Milky Way and Local Group RSGs (T. Verhoelst et al. 2009; S. de Wit et al. 2024).

In this Letter, we present pre-explosion James Webb Space Telescope (JWST) and HST imaging of the nearby SN II 2025pht discovered in NGC 1637 on 2025 June 29 by the All-Sky Automated Survey for Supernovae[11] (ASAS-SN; B. J. Shappee et al. 2014; C. S. Kochanek et al. 2017; K. Z. Stanek & S. Petz 2025). Using a post-explosion HST image of SN 2025pht, we demonstrate that this event has a single, credible counterpart in pre-explosion imaging and is detected at wavelengths from 0.8 to 8 μm in HST/WFPC2, JWST/Near Infrared Camera (NIRCam), and JWST/Mid-Infrared Instrument (MIRI) from ≈24 to 0.7 yr prior to discovery. In Section 4, we model the photometry using blackbody and realistic stellar SED models. In Section 5, we then place the SN 2025pht progenitor candidate in the context of other SN II progenitor stars and consider its high circumstellar extinction for modeling of other SN progenitor stars that lacked similar detailed mid-IR detections.

Throughout this Letter we adopt a Milky Way line-of-sight reddening of $E(B-V) = 0.036$ mag to SN 2025pht derived from E. F. Schlafly & D. P. Finkbeiner (2011). We also use the Cepheid distance of 12.03 ± 0.39 Mpc to NGC 1637 from A. Saha et al. (2006) and a redshift to NGC 1637 of $z = 0.002392$ from C. M. Springob et al. (2005).

2. Observations of SN 2025pht and Its Progenitor Candidate

2.1. Post-explosion Hubble Space Telescope Imaging

We observed the site of SN 2025pht on 2025 July 31 with WFC3/UVIS in the F336W band. We used 16×70 s (1120 s total) exposures over a single orbit, reading out only the UVIS2-C1K1C subarray and using a four-point box dither pattern around our target to maximize open shutter time. Downloading all of the `flc` frames, we processed these data using `hst123`, including frame-to-frame alignment with `TweakReg` (R. A. Lucas & B. Hilbert 2015), drizzling using `astrodrizzle` (W. J. Hack et al. 2021), and photometry of sources detected in the image frame with `dolphot` (A. Dolphin 2016). SN 2025pht is clearly detected in the output `dolphot` catalog, with a brightness of $m_{\rm F336W} = 19.06 \pm 0.01$ mag.[12]

2.2. Spectroscopy of SN 2025pht

SN 2025pht was observed with the Low-Resolution Imaging Spectrograph (LRIS; J. B. Oke et al. 1995) on the 10 m Keck I telescope on 2025 July 27.64. The 600/4000 grism was used on the blue channel, along with the 1200/7500 grating on the red channel. This setup achieves a nominal dispersion of 0.63 Å mm^{-1} between 3140 and 5640 Å and 0.4 Å mm^{-1} between 5680 and 7340 Å.

To reduce the LRIS data, we used the `UCSC Spectral Pipeline`[13] (M. R. Siebert et al. 2020), a custom data reduction pipeline based on procedures outlined by R. J. Foley et al. (2003), J. M. Silverman et al. (2012), and references therein. The two-dimensional spectra were bias corrected, flat field corrected, adjusted for varying gains across different chips and amplifiers, and then trimmed to the data section. One-dimensional spectra were extracted using the optimal algorithm (see K. Horne 1986). The spectra were wavelength calibrated using internal comparison-lamp spectra with linear

[11] SN 2025pht is also called ASASSN-25cw.

[12] All photometry reported throughout this Letter is given on the AB magnitude system (J. B. Oke & J. E. Gunn 1983).

[13] https://github.com/msiebert1/UCSC_spectral_pipeline

shifts applied via cross-correlation of the observed night-sky lines in each spectrum to a master night-sky spectrum. Flux calibration and telluric correction were also performed using standard stars observed at a similar air mass to that of the science exposures. A more detailed description of this reduction process is provided elsewhere (R. J. Foley et al. 2003; J. M. Silverman et al. 2012; M. R. Siebert et al. 2020).

2.3. Pre-explosion Hubble Space Telescope Imaging

The site of SN 2025pht was observed over several visits by HST from 1994 to 2024 with the Wide Field Planetary Camera 2 (WFPC2) and WFC3/UVIS. We downloaded the calibrated exposures[14] and produced drizzled stacks for each unique visit and filter using `hst123` (C. D. Kilpatrick 2021) following procedures described in C. D. Kilpatrick et al. (2023a). In addition, we produced deep stacks for all WFPC2 F555W and F814W images.

We obtained photometry of point sources in all HST images using `dolphot` (A. Dolphin 2016). Using our deep WFPC2/F814W stack as a reference image, we used standard `dolphot` parameters[15] to measure the brightness of faint sources near the site of SN 2025pht. We produced a final HST catalog of point sources within 10″ of the reported coordinates of SN 2025pht with a final signal-to-noise ratio of $\geqslant$3.5, `dolphot` crowding parameter $<$2, sharpness^2 $<$ 0.3, and `dolphot` quality flag $\leqslant$3.

2.4. James Webb Space Telescope Imaging

The site of SN 2025pht was observed by JWST using NIRCam and MIRI over two epochs on 2024 February 5 and October 8. We obtained all level 2 images and processed them using our custom pipeline described in P. K. Blanchard et al. (2025), including frame-to-frame alignment with `JHAT` (A. Rest et al. 2023), mosaicking each band into level 3 images using the JWST pipeline (H. Bushouse et al. 2023), and photometry of all sources in the level 2 images using `dolphot`. We applied the same `dolphot` quality cuts to the JWST catalogs as in our HST reductions.

3. Spectral Classification of SN 2025pht

3.1. Spectral Classification and Approximate Phase

We compare our Keck/LRIS spectrum of SN 2025pht with those of other SNe II using `SNID` (S. Blondin & J. L. Tonry 2011), finding the best matches to those of SN 2004et during the plateau phase. In particular, the best-fitting SN 2004et spectrum was from 2004 November 11 as originally presented in D. K. Sahu et al. (2006), which corresponds to a phase relative to their derived explosion date of ≈50 days. Overall, the broad features of hydrogen and helium are well matched as shown in Figure 1.

In order to validate the approximate the phase more quantitatively, we measure an Hα velocity from the trough of the blueshifted P Cygni absorption feature of 6800 $\pm$ 100 km s^{-1} for SN 2025pht. This is in good agreement with the measurement from SN 2004et in the best-fitting spectrum of 7000 $\pm$ 300 km s^{-1} from D. K. Sahu et al. (2006). We conclude that SN 2025pht is an SN 2004et–like Type II-P SN that was likely in its plateau phase during our 2025 July 27 observation.

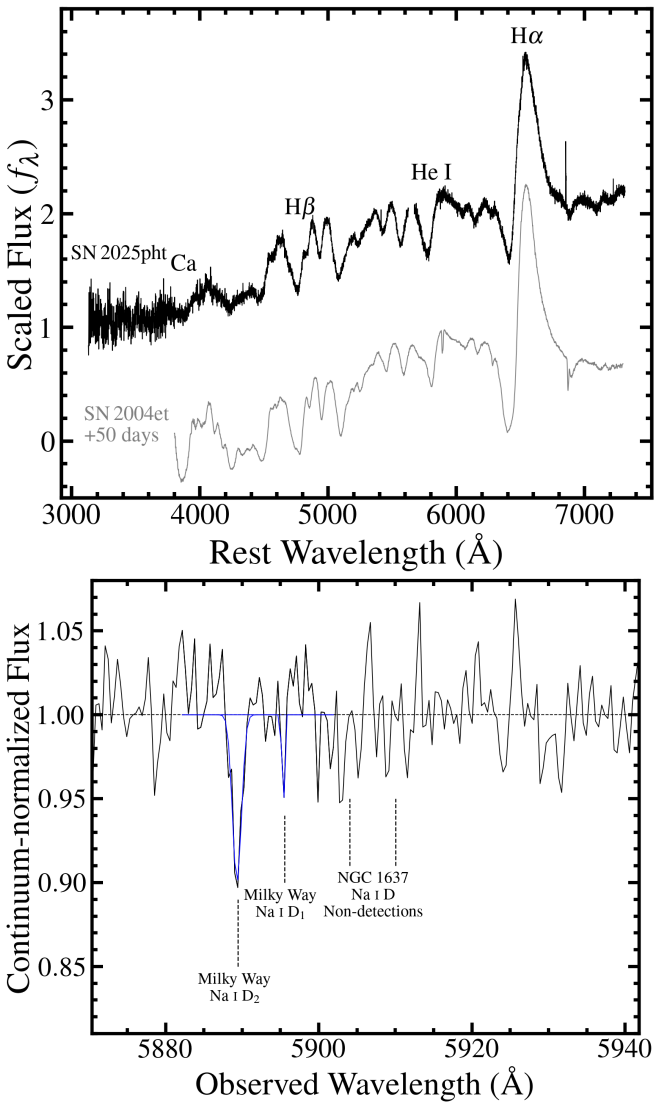

Figure 1. Top: our Keck/LRIS spectrum of SN 2025pht (black) obtained on 2025 July 27 as described in Section 2.2 and compared with a spectrum of SN 2004et (gray) that is most consistent with our observation (Section 3.1). We identify key features that aid in our classification of SN 2025pht as a typical SN II, likely in its plateau phase during this epoch and with an Hα velocity derived from the trough of its blueshifted absorption of 6800 $\pm$ 100 km s^{-1}. Bottom: a continuum-normalized section of the SN 2025pht spectrum centered on the rest wavelength of Na I D at the redshift of NGC 1637 (≈5906 Å). While we detect the Milky Way components of Na I D, we do not detect any Na I D absorption from NGC 1637, leading us to conclude that there is an insignificant magnitude of line-of-sight extinction to SN 2025pht in this galaxy. All spectra are available via WISeREP (O. Yaron & A. Gal-Yam 2012).
(The data used to create this figure are available in the online article.)

3.2. Constraints on Host Galaxy Reddening Derived from Na I D

We use our high-resolution Keck spectrum of SN 2025pht to derive a line-of-sight extinction based on Na I D lines. The equivalent width of the Na I D doublet is correlated with extinction, and stronger Na I D absorption features are observed when extinction and reddening are more pronounced. Relations that correlate Na I D absorption with extinction and reddening have been derived using spectra and light curves of quasars and

[14] That is, `c0m` files for WFPC2 and `flc` files for WFC3.
[15] Including `FitSky=2` and a final signal-to-noise threshold of `SigFinal=3.5`.

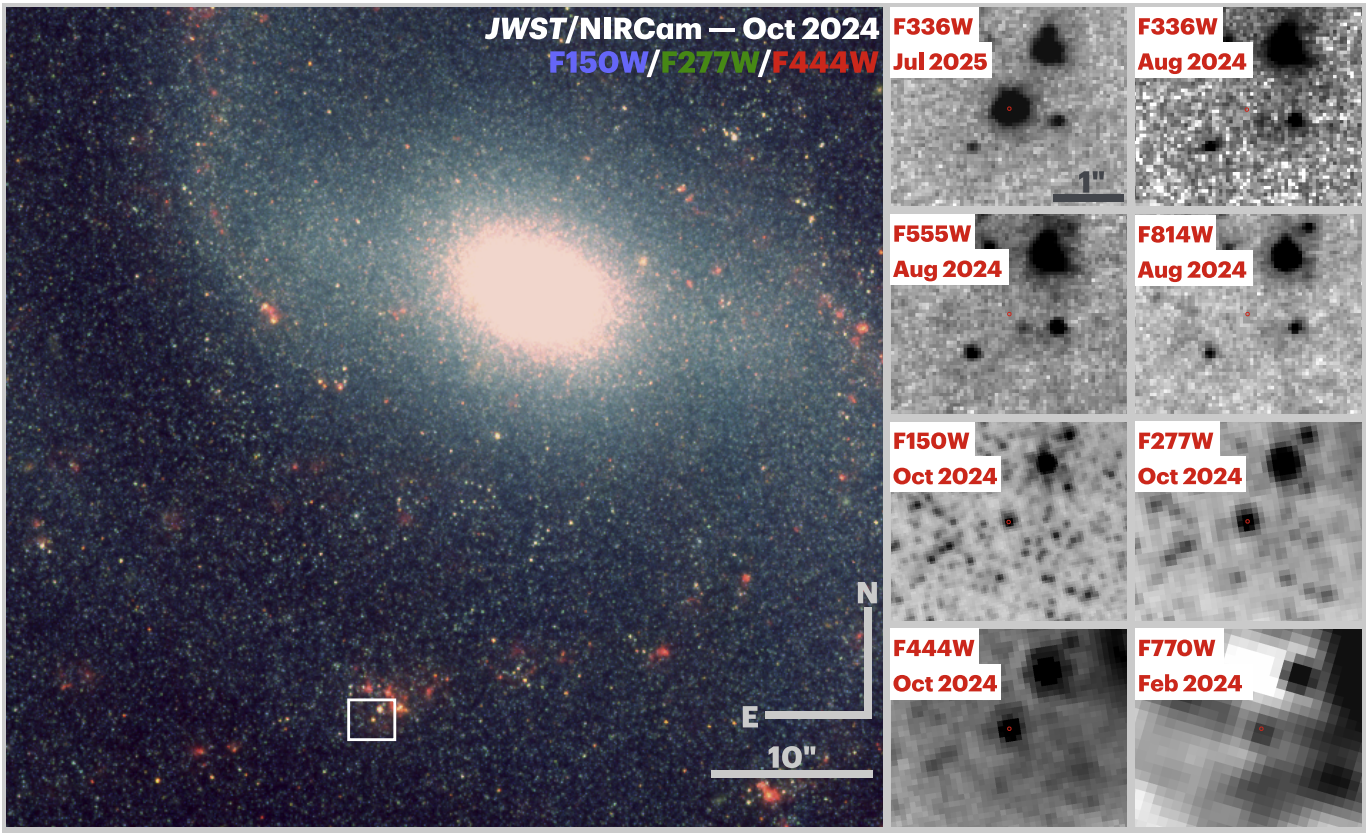

Figure 2. Left: a color image of NGC 1637 constructed from F150W (blue), F277W (green), and F444W (red) images obtained with JWST/NIRCam on 2024 October 8 showing a 1.0×0.9 arcmin^2 portion of the galaxy. We highlight a 2.7×2.4 arcsec^2 region centered on the site of SN 2025pht with a white box toward the bottom of the frame. Right: a series of grayscale frames showing HST/WFC3 F336W imaging of SN 2025pht obtained on 2025 July 31, with the centroid of the SN marked in red. We show the same region obtained by HST/WFC3 in F336W, F555W, and F814W obtained on 2024 August 3; by JWST/NIRCam in F150W, F277W, and F444W on 2024 October 8; and by JWST/MIRI on 2024 February 5. We show the location of the SN with the same red circle, demonstrating that there is a credible counterpart detected in all of the JWST images as discussed in Section 4.1.

SNe (see, e.g., D. Poznanski et al. 2012; M. M. Phillips et al. 2013; L. Galbany et al. 2016a; M. D. Stritzinger et al. 2018).

We show the continuum-normalized spectrum centered around the rest wavelength of Na I D in NGC 1637 in Figure 1. The Milky Way Na I D component is clearly observed at the appropriate rest wavelengths of 5889.95 and 5895.92 Å for Na I D_2 and Na I D_1, respectively, and we derive equivalent widths for both components of $\mathrm{EW}_{\mathrm{Na\,I\ \ D_2}} = 0.15 \pm 0.04$ Å and $\mathrm{EW}_{\mathrm{Na\,I\ \ D_1}} = 0.05 \pm 0.02$ Å. However, we do not observe any significant Na I D emission at the redshift of NGC 1637. If we force a fit at the wavelength of Na I D_2 at this redshift (i.e., with the centroid fixed at 5904.04 Å) and with the line width fixed to that of the Milky Way component (≈0.59 Å), the best-fitting equivalent width is 0.00 ± 0.02 Å, from which we infer that these lines are not detected. From the relations of D. Poznanski et al. (2012), this implies a line-of-sight host reddening of $E(B-V) < 0.02$ mag at the 3σ level. Thus, we do not apply any host extinction to the pre-explosion counterpart of SN 2025pht in the modeling below.

4. The Progenitor Candidate of SN 2025pht

4.1. Alignment between Pre- and Post-explosion Imaging and Photometry of the SN 2025pht Progenitor Candidate

We aligned our HST image of SN 2025pht to the pre-explosion JWST/NIRCam F150W image using `JHAT` (A. Rest et al. 2023). Using 36 sources common to both image frames, we applied a shift between the two image frames that minimized the rms dispersion between these two image frames. `JHAT` reported a final dispersion of 0.″030, which we adopt as the total uncertainty in the astrometric alignment between the pre- and post-explosion imaging.

Following this analysis, we compared the centroids of all sources detected by `dolphot` in the HST and JWST images around the locations shown in Figure 2. SN 2025pht is clearly visible in the F336W imaging based on comparison to the pre-explosion F336W image (Figure 2) with negligible astrometric uncertainty on its centroid located at $\alpha_{\mathrm{J2000}} = 4^{\mathrm{h}}41^{\mathrm{m}}28\overset{\mathrm{s}}{.}8767$ and $\delta_{\mathrm{J2000}} = -2°51'55\overset{''}{.}881$ in the Gaia-aligned HST image frame. Comparing to sources in our JWST catalog, there is a single, bright, point-like object in F150W whose centroid is located at $\alpha_{\mathrm{J2000}} = 4^{\mathrm{h}}41^{\mathrm{m}}28\overset{\mathrm{s}}{.}8758$ and $\delta_{\mathrm{J2000}} = -2°51'55\overset{''}{.}871$, implying an offset of 0.″017 (0.6σ). We conclude that these sources are astrometrically coincident to the level of precision of our frame-to-frame alignment and the F150W source is consistent with being the pre-explosion counterpart to SN 2025pht.

This source is detected across every pre-explosion JWST/NIRCam image, in all pre-explosion WFPC2/F814W imaging from 2001 (Figure 3), and in JWST/MIRI F770W as shown in Figure 2. In every other image, we set an approximate limiting magnitude using a forced aperture at the site of SN 2025pht set to the 95% encircled energy radius in each band with the appropriate zero-point and aperture correction. All detections

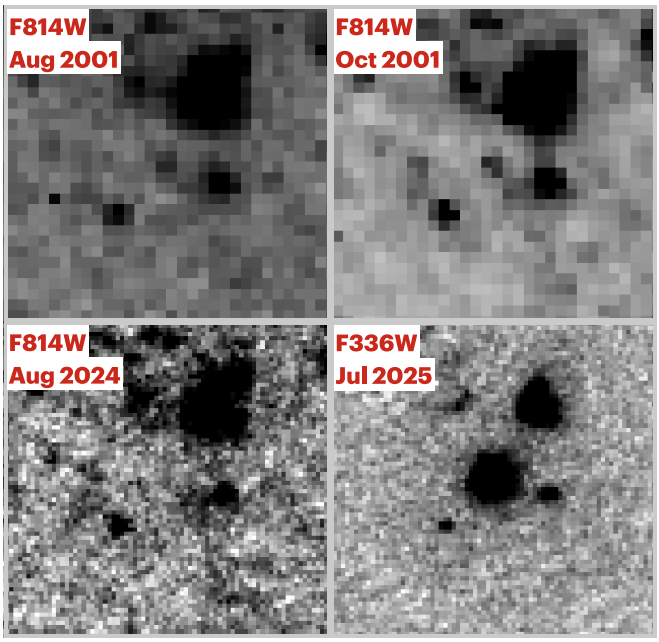

Figure 3. A series of HST/WFPC2 (top) and WFC3 (bottom) images in F814W and F336W showing the detection of SN 2025pht (bottom right) and the detection of its counterpart from 2001 and eventual disappearance in 2024, demonstrating that the pre-explosion counterpart had some long time baseline variability over this 23 yr span. We discuss the significance of this measurement in Section 4.2.

and upper limits across each image are reported in Tables 1 and 2 for HST and JWST, respectively.

We also consider the possibility that the pre-explosion counterpart to SN 2025pht was detected owing to chance coincidence and set an approximate probability of chance coincidence using the following method. There are 417 sources within a 3″ radius of the site of SN 2025pht and detected at $>5\sigma$ in the F150W image that also pass the quality cuts we describe to the `dolphot` catalog in Section 2.4. Thus, for any source found near the location of SN 2025pht, there is roughly a 4% chance that it would be detected within 1σ of the location of an arbitrary source. We consider this to be a small but nonnegligible chance that the counterpart was detected by chance, although we do not impose any other cuts (e.g., on color, brightness, or counterparts in other catalogs) that could be used to simulate the detection of a likely SN II counterpart. Furthermore, we can validate whether the counterpart is the SN progenitor star through its eventual disappearance (similar to S. D. Van Dyk et al. 2023b).

Throughout the remainder of this Letter, we proceed under the assumption that the detected counterpart is the progenitor star of SN 2025pht and its photometry is accurately described by the values in Tables 1 and 2. However, we note that the F164N, F212N, and F405N detections ([Fe II], H_2, and Brα emission), while also coincident with the pre-explosion counterpart, are moderately brighter than the wide-band detections that are closest in wavelength (F150W, F200W, and F444W, respectively). The counterpart is also detected in F187N (Paα), but this detection is nominally fainter than in F200W, implying a low line flux. Assuming a relatively flat continuum at these wavelengths, with the rest of the emission dominated by spectral lines, we derive integrated line fluxes of $f_{[\mathrm{FeII}]} = 2.4$ μJy, $f_{\mathrm{H_2}} = 3.1$ μJy, and $f_{\mathrm{Br}\alpha} = 0.61$ μJy. This emission could plausibly arise from the circumstellar environment around the progenitor star (similar to the molecular outflows observed in RSGs such as NML Cyg; E. De Beck et al. 2025) or an unassociated nebula. However, as the detailed radiative transfer calculations that can accurately model this line flux are beyond the scope of this Letter, we do not use any narrowband photometry in the analysis below.

Table 1
HST Photometry of the SN 2025pht Progenitor Candidate

MJD	Instrument	Band	Magnitude (AB mag)	Uncertainty (mag)
49606.190	WFPC2	F606W	>24.87	⋯
52133.332	WFPC2	F450W	>25.09	⋯
52133.342	WFPC2	F814W	25.23	0.34
52154.191	WFPC2	F814W	25.16	0.24
52162.951	WFPC2	F814W	25.06	0.23
52178.531	WFPC2	F814W	25.09	0.24
52181.874	WFPC2	F814W	25.15	0.24
52184.671[a]	WFPC2	F555W	>26.61	⋯
52200.658	WFPC2	F814W	25.20	0.24
52213.625	WFPC2	F814W	25.06	0.23
60520.061	WFC3/UVIS	F657N	>24.55	⋯
60525.579	WFC3/UVIS	F814W	>26.05	⋯
60525.584	WFC3/UVIS	F438W	>26.58	⋯
60525.590	WFC3/UVIS	F336W	>25.31	⋯
60525.596	WFC3/UVIS	F275W	>26.85	⋯
60525.605	WFC3/UVIS	F555W	>26.59	⋯

Note. The MJD corresponds to the time at the start of each HST image. All photometry is on the AB magnitude scale, and limiting magnitudes are provided at 3σ as described in Section 4.1.
[a] This WFPC2 epoch is a deep stack of 12×2200 s F555W exposures obtained from 2001 September 2 to October 31. The MJD provided is the average of the start dates for each exposure.

Table 2
JWST Photometry of the SN 2025pht Progenitor Candidate

MJD	Instrument	Band	Magnitude (AB mag)	Uncertainty (mag)
60345.633	MIRI	F0770W	21.25	0.11
60345.639	MIRI	F2100W	>17.04	⋯
60345.679	NIRCam	F150W	22.12	0.01
60345.679	NIRCam	F300M	21.13	0.01
60345.688	NIRCam	F187N	21.94	0.02
60345.688	NIRCam	F335M	20.96	0.01
60591.272	NIRCam	F187N	21.99	0.02
60591.272	NIRCam	F405N	20.84	0.01
60591.299	NIRCam	F164N	21.70	0.02
60591.299	NIRCam	F335M	21.01	0.01
60591.326	NIRCam	F212N	21.26	0.01
60591.326	NIRCam	F360M	20.89	0.01
60591.352	NIRCam	F150W	22.31	0.01
60591.352	NIRCam	F444W	20.88	0.01
60591.370	NIRCam	F200W	21.60	0.01
60591.370	NIRCam	F277W	21.43	0.01

Note. The MJD corresponds to the time at the start of each JWST image. All photometry is on the AB magnitude scale, and limiting magnitudes are provided at 3σ as described in Section 4.1.

4.2. Evidence for Variability from the SN 2025pht Progenitor Candidate

Motivated by previous studies of extreme variability in SN II progenitor candidates (e.g., SN 2020tlf and SN 2023ixf,

which exhibited some level of pre-explosion optical or mid-IR variability; W. V. Jacobson-Galán et al. 2022; J. E. Jencson et al. 2023; C. D. Kilpatrick et al. 2023a; M. D. Soraisam et al. 2023), we quantify whether the SN 2025pht counterpart exhibits similar evidence for detectable variability in the optical and mid-IR. We have three avenues of investigation to quantify this for the SN 2025pht counterpart: (i) the seven epochs of WFPC2/F814W photometry from 2001 August 12 to October 31, (ii) the difference between these epochs and the 2024 August 3 WFC3/F814W photometry, and (iii) the two epochs of NIRCam/F150W and F335M photometry on 2024 February 5 and October 8.

For the former, the low signal-to-noise ratio of the individual WFPC2/F814W detections (e.g., in Figure 2) precludes any strong statement on the intrinsic variability of the underlying source. Over this 80-day period, the source was less variable than the peak-to-peak difference combined with the individual statistical uncertainties on each measurement, or $\lesssim$0.3 mag. On the other hand, the difference between the detection in 2001 and nondetection in 2024 is more extreme, with a 0.84 mag (factor of 2.2) decline in brightness. While there are examples of stars with similar levels of variability at these wavelengths (α Ori had similar peak-to-peak variability from 2017 to 2019 at these wavelengths; D. Taniguchi et al. 2022), the 0.84 mag decline is only a lower limit on our knowledge of the counterpart's variability and already makes the counterpart among the most extreme $M_I < -5$ mag variables observed on timescales of decades (e.g., those in M51 in C. Conroy et al. 2018).

Finally, the level of variability measured in F150W (+0.19 mag) and F335M (+0.05 mag) is weak compared with extreme IR sources such as the SN 2023ixf counterpart. Although we only measure this source in two epochs and cannot firmly conclude that we have captured the full range of changes in this source, we do not see any strong evidence for changes on this timescale of 246 days (roughly 1/4 the period derived from variability in SN 2023ixf; C. D. Kilpatrick et al. 2023a).

For the purposes of our analysis and given the lack of strong variability in the observations from 2024, we consider the $m_{\rm F814W} > 26.05$ mag WFC3/UVIS limit to be nearly contemporaneous with the NIRCam and MIRI detections. Therefore, in the modeling of this source's SED below, we adopt this limit in F814W as opposed to the prior detections from 2001.

4.3. The Spectral Energy Distribution of the SN 2025pht Progenitor System

4.3.1. Blackbody Spectral Energy Distributions

We first fit broadband photometry of the SN 2025pht pre-explosion counterpart with a blackbody model. We forward-model SEDs of a fixed luminosity ($\log(L/L_\odot)$) and effective temperature ($T_{\rm eff}$) using realistic bandpasses for each JWST and HST filter and using `synphot` (P. Lian Lim 2020) to derive the expected brightness of the counterpart. We adopt the distance and redshift given above and assume the E. L. Fitzpatrick (1999) extinction law for Milky Way dust via the `extinction` module (K. Gordon 2024). As described in Section 3.2, we assume zero host extinction.

We fit this model using `emcee` (D. Foreman-Mackey et al. 2013) by optimizing the likelihood function:

$$\log \mathscr{L}(\theta) = -\frac{1}{2}\sum_i \left(\frac{(m_{i,\rm obs} - m_{i,\rm model}(\theta))^2}{\sigma_i^2 + \sigma_{\rm sys}^2} + \log(2\pi(\sigma_i^2 + \sigma_{\rm sys}^2)) \right), \quad (1)$$

where $m_{i,\rm obs}$ is an observed magnitude and σ_i is its corresponding uncertainty, $m_{i,\rm model}$ is a magnitude derived from our forward model for input model parameters θ in that observation's bandpass, and $\sigma_{\rm sys}$ is a systematic uncertainty term that we fit for to account for additional variance in the data (e.g., due to unmodeled variability) or other systematic uncertainties in the model.

We run our blackbody model for 5000 steps after an initial burn-in of 1000 steps and using 100 walkers, and from the samples on our `emcee` chains, we report the median and 16th and 84th percentile model parameters from the output posteriors as our best-fitting and 1σ uncertainty range on each parameter. For this run, the best-fitting parameters are $\log(L/L_\odot) = 4.96^{+0.10}_{-0.09}$, $T_{\rm eff} = 1470 \pm 40$ K, and $\sigma_{\rm sys} = 0.212^{+0.060}_{-0.046}$ mag. The luminosity contains the added systematic uncertainty on the distance, although we do not include these values in our fit since the uncertainty is correlated across the SED and our model magnitudes are simply scaled to the correct distance.

Similar to SN 2023ixf (J. E. Jencson et al. 2023; C. D. Kilpatrick et al. 2023a), SN 2022acko (S. D. Van Dyk et al. 2023a), and SN 2024ggi (D. Xiang et al. 2024), all of which had a pre-explosion counterpart detected in multiple bands, including at >1 μm, the blackbody temperature implied by the pre-explosion counterpart photometry is much cooler than any known supergiant photosphere. We therefore infer that there must be an extended mass of CSM beyond the SN 2025pht progenitor star in which a cooler photosphere forms, roughly at the derived blackbody radius of $\approx$3700 $R_\odot$. Assuming that the counterpart is an RSG with a total $\log(L/L_\odot) = 4.96$ ($M_{\rm ZAMS} \approx 14.5\ M_\odot$ assuming a MIST single-star model; J. Choi et al. 2016), the photosphere would be 5.3 times as large as the underlying star, suggesting an optically thick, dusty source that forms in a dense RSG wind. We therefore turn to a more sophisticated SED to constrain the properties of both this material and the underlying star.

4.3.2. Red Supergiant Spectral Energy Distributions

We consider SED models based on realistic spectra of RSGs derived from MARCS (B. Gustafsson et al. 2008) and fully passed through the radiative transfer code `dusty` (Z. Ivezic & M. Elitzur 1997) to describe the SN 2025pht progenitor star. We take MARCS SEDs corresponding to RSGs with effective temperatures $T_{\rm eff}$ = 2600–5000 K and scaled to luminosities from $\log(L/L_\odot) = 3.0$ to 5.8. All of these SEDs were calculated at solar metallicity, which is the closest available model to the global metallicity in NGC 1637 of $\log[{\rm Fe/H}] = -0.11$ (L. Galbany et al. 2016b). We then model a dust-obscured RSG by processing each SED through a model dust shell containing dust with a grain size (a) distribution of $dn/da \propto a^{-3.5}$ (i.e., a MRN distribution; J. S. Mathis et al. 1977) from $a = 0.005$ to 0.25 μm. The shell has a fixed

effective temperature from 500 to 1500 K and an optical depth at 5500 Å of $\tau_V = 0.01$–15.0. The geometry of the dust shell follows a density profile with $\rho(r) \propto r^{-2}$ and an outer radius ($R_{\rm out}$) fixed to $2R_{\rm in}$, where the inner radius $R_{\rm in}$ is degenerate with τ_V and is not explicitly defined. We note that, based on our estimate of the phase of SN 2025pht above and the fact that there was no appreciable Na I D absorption at ≈50 days from explosion, we can set an approximate upper limit on the size of the dust shell. We assume that the initial ejecta velocity was ≈10,000 km s^{-1} (which is high for typical SNe II; L. Martinez et al. 2022), implying that at a radius of at most ≈62,000 $R_\odot$ there was no circumstellar extinction, and thus we can limit possible values of $R_{\rm out}$.

Finally, we consider two compositions that define the dust grain abundances and their corresponding opacities from B. T. Draine & H. M. Lee (1984): a pure graphite model and a pure silicate model. We fit these dust composition models separately, but otherwise we allow the model parameters ($\log(L/L_\odot)$, $T_{\rm eff}$, $T_{\rm dust}$, τ_V) to vary within the bounds described above.

Following a similar fitting method to that of the blackbody model, we ran our graphitic model for 25,000 steps with a 5000-step burn-in with 100 walkers and found a best-fitting model with $\log(L/L_\odot) = 5.00^{+0.09}_{-0.08}$, $T_{\rm eff} = 3030^{+210}_{-270}$ K and enshrouded in a dust shell with $T_{\rm dust} = 790^{+40}_{-30}$ K and $\tau_V = 6.7 \pm 0.4$. The final systematic variance was $\sigma_{\rm sys} = 0.08^{+0.03}_{-0.02}$ mag.

Similarly, we fit the silicate model to the pre-explosion photometry, but the model did not converge, and all of the walkers ended at the edge of the opacity boundary with $\tau_V = 15$. We increased this parameter to allow for models with $\tau_V = 0.01$–100 and performed the same fit again, with the best-fitting model exhibiting $\log(L/L_\odot) = 5.01 \pm 0.09$, $T_{\rm eff} = 2800^{+450}_{-150}$ K, $T_{\rm dust} = 1360^{+90}_{-100}$ K, and $\tau_V = 22.8^{+2.1}_{-2.4}$ with $\sigma_{\rm sys} = 0.15^{+0.05}_{-0.04}$ mag (Figure 4). However, we note that the model predicts a significantly higher MIRI/F770W flux than the observation, which is inconsistent with the detection at the $>3\sigma$ level. This inconsistency does not occur with the graphitic model, which has a smoother continuum and is well matched to the MIRI/F770W observation. We emphasize that there is a clear feature at these wavelengths associated with silicate-rich dust (B. T. Draine & H. M. Lee 1984), which is often used to distinguish between dust compositions in the spectra of RSGs (e.g., J. T. van Loon et al. 2005; T. Verhoelst et al. 2009; J. T. van Loon 2025).

Although, superficially, this mismatch between the model and photometry would appear to imply that τ_V is overestimated, when we perform the same silicate-rich model fit using only the NIRCam photometry, we derive $\tau_V = 19.2^{+3.1}_{-2.7}$ with a similarly prominent silicate feature to that shown in Figure 5. This model largely captures the shape of the short-wavelength SED, suggesting that it is primarily the NIRCam photometry driving the high-opacity prediction for silicate-rich dust models. Similarly, we derive $\tau_V = 6.3$ for the graphitic model in this NIRCam-only fit, consistent with the value derived above, indicating that this model can accurately predict the MIRI/F770W flux even if we do not include that observation in our `emcee` fit.

We next consider the possibility that although the $\sigma_{\rm sys}$ value derived from the silicate-rich fit is comparable to the level of observed variability in F150W and F335M in Section 4.2, the variability in F770W could be larger, and thus combining photometry over a ≈8-month period is not representative of the underlying SED (similar to SN 2023ixf; J. E. Jencson et al. 2023; C. D. Kilpatrick et al. 2023a). We perform a new fit by restricting the model to constrain only wide-band detections obtained on 2024 February 5 (Figure 5), which were observed within the span of ≈2 hr and are therefore unlikely to be significantly affected by variability in any RSG (whose characteristic variability timescales are months to years; M. D. Soraisam et al. 2018). Again, the model predicts a large $\tau_V = 22.7^{+0.6}_{-0.8}$ with a much higher flux in F770W than we observe.

Finally, we consider the possibility that our choice of the dust shell width has some effect on the observed level of dust opacity and associated emission in the F770W band. We try a new fit with a moderately extended dust shell where $R_{\rm out} = 10R_{\rm in}$. The overall opacity prediction remains high at $\tau_V = 26.1$, and the model remains inconsistent with the F770W detection at $>3\sigma$, whereas the graphitic model is consistent with the data for this dust shell width. Moreover, the dust shell cannot be significantly wider than this, as the radius predicted by this silicate model is $R_{\rm in} = 5240\ R_\odot$, implying that the outer radius 52,400 $R_\odot$ is approaching our limit on the size of the dust shell from spectroscopy.

We therefore conclude that the SN 2025pht counterpart photometry is consistent with an RSG enshrouded in a graphitic dust shell and inconsistent with silicate-rich circumstellar dust. The underlying RSG is robustly predicted as having $\log(L/L_\odot) = 5.0$ owing to the excellent sampling of the SED, even within relatively narrow time windows. Our best-fitting graphitic model predicts a moderately high optical opacity of $\tau_V = 6.7$, which corresponds to $A_V = 5.3$ mag of circumstellar extinction due to the dust shell. We discuss these conclusions and the implications for RSG modeling and SN progenitors below.

5. Discussion

The SN 2025pht progenitor candidate is on the high-luminosity end of RSG counterparts to nearby SNe II observed to date, although not the most luminous system observed (which is likely SN 2009hd at $\log(L/L_\odot) = 5.24$; S. Healy et al. 2024) or beyond the "maximum luminosity" predicted in analyses of the RSG problem (e.g., in S. J. Smartt 2009; C. S. Kochanek 2020; E. R. Beasor et al. 2025). Nevertheless, compared with the vast majority of SN II pre-explosion counterparts, which are often detected in only a single band, its luminosity is robustly constrained via detections from WFPC2/F814W to MIRI/F770W, roughly an order of magnitude in wavelength. In particular, constraints on the magnitude and nature of dust emission in the circumstellar environment around this source are more tightly constrained than almost any other SN II progenitor candidate (e.g., in S. J. Smartt 2015; C. D. Kilpatrick & R. J. Foley 2018; S. D. Van Dyk et al. 2018; J. E. Jencson et al. 2023; C. D. Kilpatrick et al. 2023a).

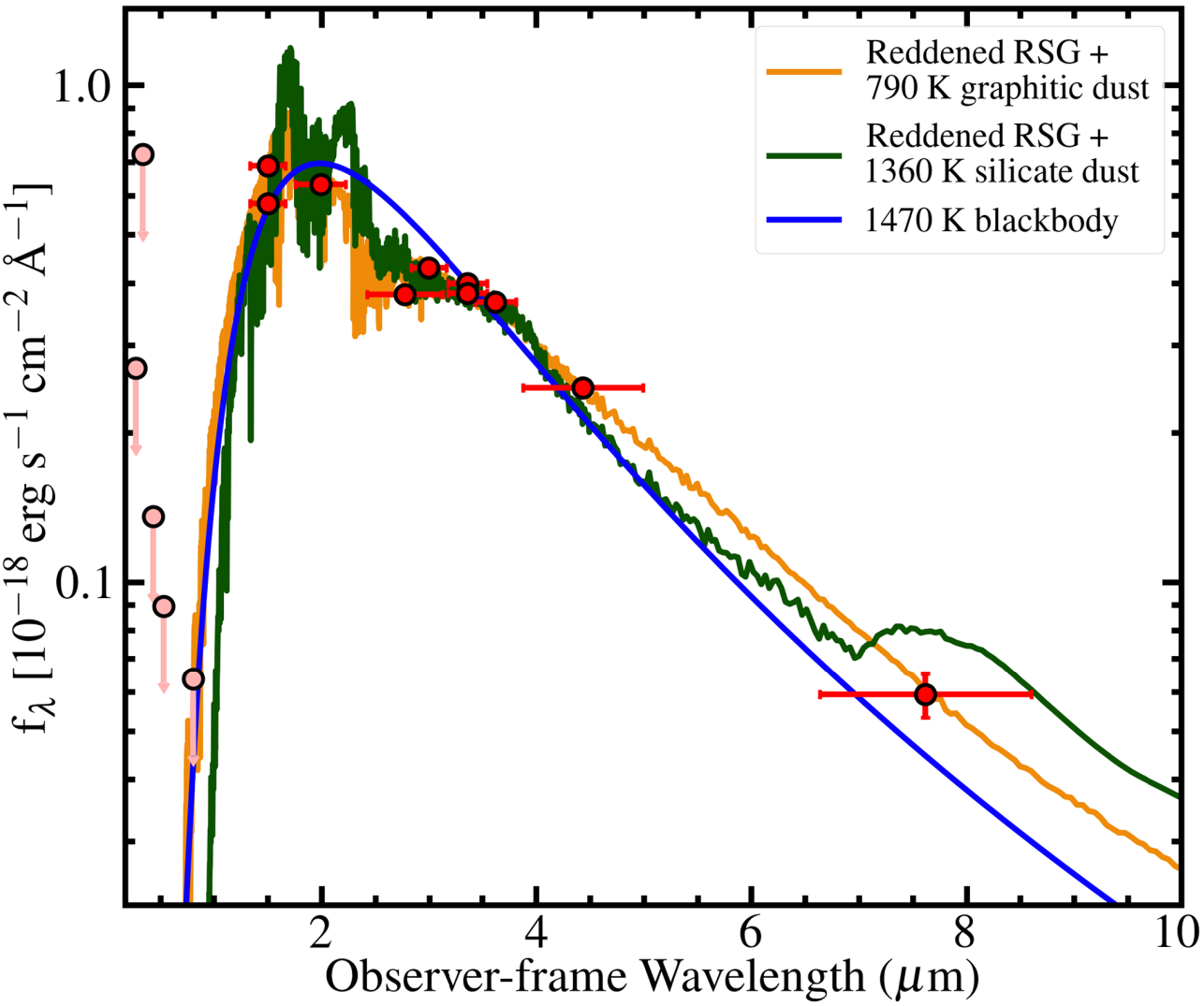

Figure 4. Our best-fitting SEDs to the 2024 detections of the SN 2025pht counterpart as discussed in Section 4.3. All SEDs correspond to a source with $\log(L/L_\odot) \approx 5.0$. Motivated by the cool blackbody fit, we attempt fits to MARCS SEDs of RSGs reddened via dust prescriptions using `dusty` as described in Section 4.3.2. While a purely graphitic dust prescription captures the overall shape of the SED out to 8 μm, the silicate model overpredicts this measurement, leading us to conclude that the SN 2025pht counterpart is consistent with a graphitic dust model.

5.1. Carbon-rich Dust in the Circumstellar Environment of SN 2025pht

SN 2025pht is consistent with a $\log(L/L_\odot) = 5.0$ RSG, which at the metallicity of its host galaxy would imply a single star with an initial mass $M_{\rm ZAMS} = 15\ M_\odot$ (J. Choi et al. 2016). In general, RSGs in this mass range and above exhibit silicate-rich dust profiles based on spectroscopy (T. Verhoelst et al. 2009). However, photometric fitting for larger populations of RSGs in M31 and M33 that includes near-IR and Wide-field Infrared Survey Explorer mid-IR photometry indicates that carbon-rich dust is rarer but still observed for some RSGs in this luminosity range (T. Wang et al. 2021). Overall, the RSGs in these population studies span a relatively narrow range in temperature and metallicity, and so we infer that differences in the composition of their circumstellar dust are largely driven by their surface abundances (as in A. Lançon et al. 2007) as opposed to their environments or the relative fragility of dust grains to the star's spectrum.

In general, carbon-rich dust molecules require a circumstellar C/O ratio greater than 1 such that carbon atoms are left over after the formation of carbon monoxide (B. D. Savage & J. S. Mathis 1979). B. Davies & L. Dessart (2019) argue that as we look at higher-$M_{\rm init}$ stars, their larger convective cores will in turn yield a larger fraction of CNO-processed material in the envelope of the star at the onset of core He burning and the RSG phase. This implies that the mass fraction of carbon will be depleted, and thus we expect monotonically decreasing C/N and C/O ratios with respect to $M_{\rm init}$, which would yield a higher fraction of stars with silicate-rich circumstellar environments at the point of core collapse. This effect can be mitigated somewhat by assumptions of rotation and convective overshoot (A. Maeder & G. Meynet 2000; S. Ekström et al. 2012), and so we emphasize that the final C/O ratio is uncertain by nearly 1 dex even in B. Davies & L. Dessart (2019). Moreover, the fact that some RSGs in this luminosity range exhibit graphitic dust is evidence that their surface carbon abundances can be large.

On the other hand, we note that flash spectra of SNe II favor stars with surface abundances $\rm C/N < 1$ and $\rm C/O < 1$ (see L. Dessart & W. V. Jacobson-Galán 2023; W. V. Jacobson-Galán et al. 2023, 2024; L. Dessart 2025), in agreement with the values

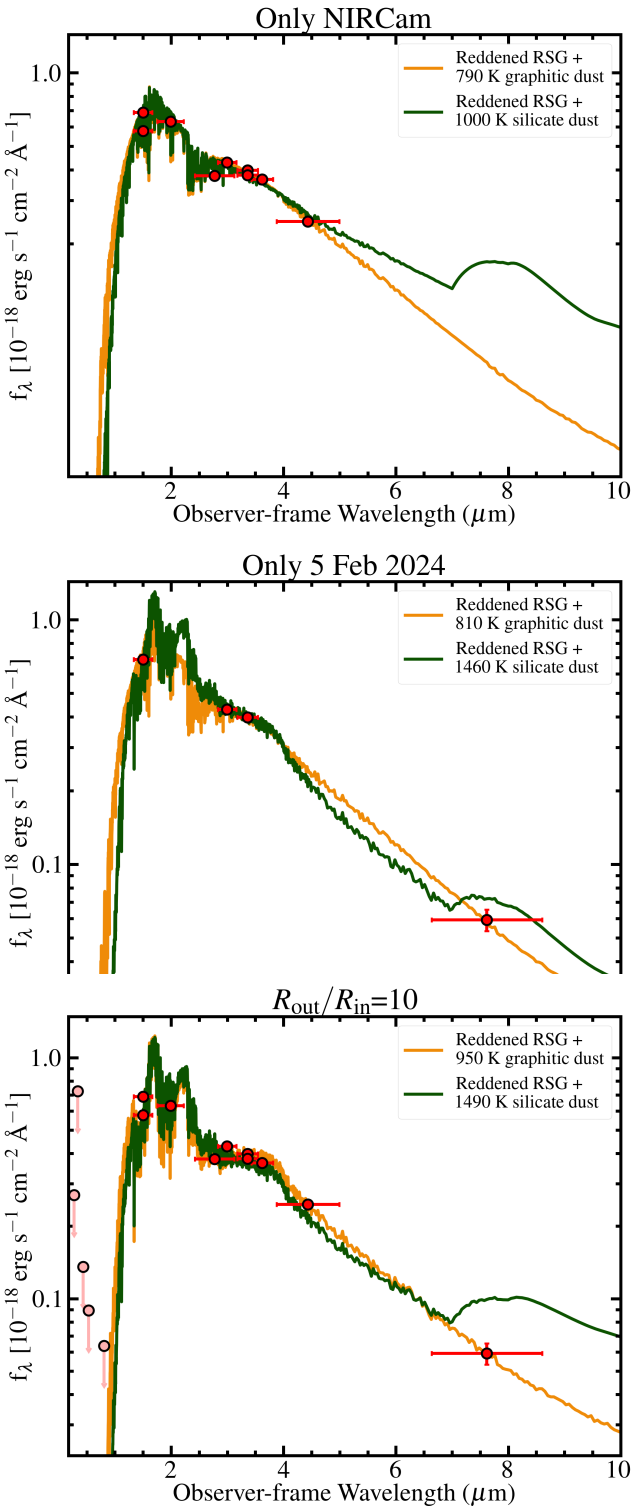
Only NIRCam
Reddened RSG + 790 K graphitic dust
Reddened RSG + 1000 K silicate dust
Only 5 Feb 2024
Reddened RSG + 810 K graphitic dust
Reddened RSG + 1460 K silicate dust
R_{out}/R_{in}=10
Reddened RSG + 950 K graphitic dust
Reddened RSG + 1490 K silicate dust
f_λ [10^{-18} erg s^{-1} cm^{-2} Å^{-1}]
Observer-frame Wavelength (μm)

Figure 5. Top: same as Figure 4, but for graphitic and silicate dust models fit only to the JWST/NIRCam photometry. This model results in similar posteriors to the full SED fit. Middle: same as the top panel, but using only JWST/NIRCam and MIRI photometry from 2024 February 5 to minimize the effects of variability. The posteriors for the silicate model still overpredict the F770W flux. Bottom: same as Figure 4, but setting the dust shell boundaries using $R_{out}/R_{in} = 10$ in our model as described in Section 4.3.2. The silicate model again overpredicts the F770W flux.

predicted by B. Davies & L. Dessart (2019). In light of these data, a high fraction of terminal RSGs with enhanced C/N and C/O ratios in the ≈12–15 $M_\odot$ mass range would be intriguing, especially as they are not expected to undergo the post He-burning dredge-up that produces carbon stars in lower mass ranges (e.g., for stars <9.2 $M_\odot$; D. Sugimoto & K. Nomoto 1980; M. Limongi et al. 2024). We note, however, that the presence of dense CSM confined closely around a large fraction of SNe II (based on light-curve modeling and flash spectroscopy; D. Khazov et al. 2016; F. Förster et al. 2018; V. Morozova et al. 2018; R. J. Bruch et al. 2021) suggests an energetic mechanism that can release a large fraction of the star's mass (e.g., a "superwind" or outburst as in V. Morozova et al. 2020; B. Davies et al. 2022; J. Fuller & D. Tsuna 2024). If this mechanism is energetic enough to initiate post He-burning dredge-up from the base of the RSG's convective envelope, it could simultaneously explain both the presence and composition of the CSM around SN progenitor stars similar to SN 2025pht. Future studies that analyze the correlation between the mass and composition of this material may offer a way to determine its exact origin in the progenitor system.

5.2. The High Optical Opacity toward the SN 2025pht Counterpart and Implications for the Red Supergiant Problem

As discussed above, the vast majority of SN II pre-explosion counterparts are observed in F814W as the reddest (and sometimes only) band in their SEDs (see joint analyses in S. J. Smartt 2009, 2015; B. Davies & E. R. Beasor 2018; C. S. Kochanek 2020; S. Healy et al. 2024). This places a significant systematic uncertainty on their bolometric corrections when taking into consideration that their optical opacities can be as high as that of SN 2025pht. We underscore this point here by comparing bolometric corrections from the recent joint analysis in S. Healy et al. (2024) to the values we infer from well-sampled SN progenitor star SEDs.

S. Healy et al. (2024) derive F814W, I_c-band (Cousins), I_j-band (Johnson), or i-band (SDSS) bolometric corrections for 22/30 SN pre-explosion counterparts, including uncertainties. We treat these bands as being comparable in wavelength and model the probability density functions (pdf's) of their bolometric corrections as Gaussian distributions with the given means and standard deviations in S. Healy et al. (2024). We show the joint pdf for 20 of these sources (discounting SN 2023ixf and 2024ggi) in Figure 6. For comparison, we show the bolometric corrections for SN 2017eaw (C. D. Kilpatrick & R. J. Foley 2018), SN 2023ixf (C. D. Kilpatrick et al. 2023a), SN 2024ggi (D. Xiang et al. 2024), and SN 2025pht (this Letter), which were selected since their counterparts have >2 μm detections from Spitzer/IRAC or JWST. We model these bolometric corrections by running the same reddened RSG model described in Section 4.3.2 for MARCS SEDs surrounded by a graphitic, $R_{out}/R_{in} = 2$ dust shell (see the derived model parameters in Table 3). Each bolometric correction we derive is modeled to the WFC3/UVIS F814W band by taking 10^5 samples from the model posteriors and calculating $M_{bol} - M_{F814W}$, which we show in Figure 6. We emphasize that since the four objects we analyze all have well-constrained SEDs from optical to mid-IR wavelengths, their bolometric corrections are relatively insensitive to the choice of dust model, and our conclusions below depend solely on the derived luminosities.

We caution that the four objects we analyze may not be representative of the overall SN II population, due to selection effects associated with requiring >2 μm detections (although many other sources have constraining upper limits at these

Table 3
Derived Parameters for the SN 2025pht Progenitor Star and Other Progenitor Stars from the Literature

SN Name	$\log(L/L_\odot)$	$T_{\rm eff}$ (K)	$T_{\rm dust}$ (K)	τ_V	$\sigma_{\rm sys}$ (mag)	References
2025pht	$5.00^{+0.09}_{-0.08}$	3030^{+210}_{-270}	790^{+40}_{-30}	6.7 ± 0.4	$0.08^{+0.03}_{-0.02}$	(this Letter)
2017eaw	4.90 ± 0.08	3310^{+40}_{-30}	910^{+300}_{-280}	1.2 ± 0.4	$0.13^{+0.06}_{-0.04}$	[1]
2023ixf	$4.73^{+0.10}_{-0.08}$	4000^{+330}_{-290}	1180^{+130}_{-120}	5.8 ± 0.3	$0.09^{+0.10}_{-0.06}$	[2]
2024ggi	4.85 ± 0.12	3280^{+70}_{-110}	660^{+200}_{-120}	$1.6^{+0.4}_{-0.5}$	$0.32^{+0.05}_{-0.04}$	[3]

Note. The derived model parameters from running our graphitic, $R_{\rm out}/R_{\rm in} = 2$ RSG dust model as described in Section 4.3.2 for SN 2025pht and several SN progenitors, with photometry presented in the literature. The photometry comes from the provided references. **References.** (1) C. D. Kilpatrick & R. J. Foley (2018); (2) C. D. Kilpatrick et al. (2023a); (3) D. Xiang et al. (2024).

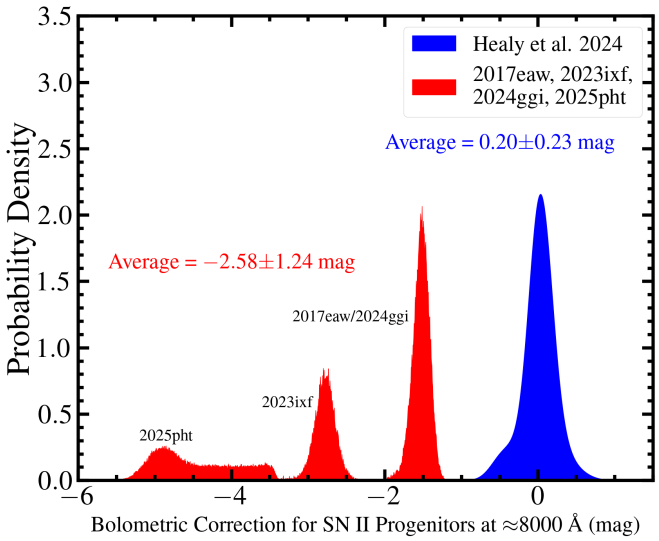

Figure 6. The probability density for the bolometric correction to ≈8000 Å (i.e., for F814W, I_c, I_j, and i bands) for 20 pre-SN counterparts to SNe II from S. Healy et al. (2024; blue; see their Table A.2) compared with the bolometric correction derived for WFC3/UVIS F814W in our modeling of SN 2017eaw, SN 2023ixf, SN 2024ggi, and SN 2025pht (red; see Section 5.2). As the latter events have well-sampled SEDs, including at >2 μm with Spitzer and JWST, we consider their optical bolometric corrections, where most SN II counterparts are detected to be more reliable than for SN II counterparts that lack IR photometry. We measure the average and standard deviation of both distributions as 0.20 ± 0.23 mag and -2.58 ± 1.24 mag.

wavelengths, e.g., for SN 2020jfo; C. D. Kilpatrick et al. 2023b) or from possible biases in the photometry used, our modeling, or the more systematic modeling in studies such as S. Healy et al. (2024). However, we note that these four sources all have systematically larger bolometric corrections than those analyzed in the literature. We infer that a significant fraction of the sources with only F814W detections are actually much more luminous than assumed (similar to conclusions in E. R. Beasor et al. 2025). If we consider the difference between the average of the distribution of bolometric corrections we calculate and those from S. Healy et al. (2024), which is 2.78 ± 1.26 mag or 1.1 ± 0.50 dex in luminosity, a correction even on the lower side of this distribution could place low-luminosity SN II counterparts (such as SN 2003gd or SN 2020jfo, with $\log(L/L_\odot) = 4.3$ and $\log(L/L_\odot) = 4.1$, respectively; J. J. Eldridge & C. A. Tout 2004; J. Sollerman et al. 2021; R. S. Teja et al. 2022; C. D. Kilpatrick et al. 2023b) above the "maximum" luminosity counterpart of $\log(L/L_\odot) = 5.2$. Thus, we emphasize that more detailed modeling of all such RSG counterparts is warranted in light of the strong priors on high circumstellar extinction from more recent SN II progenitor star detections.

5.3. Caveats to Our Inferences on the Nature of the SN 2025pht Progenitor and Future Direction

The conclusions listed above for SN 2025pht assume a fixed dust abundance profile with only two opacity laws from B. T. Draine & H. M. Lee (1984), a spherical shell following an r^{-2} wind profile within fixed radii, and an arbitrary dust grain size distribution, and we largely ignore the effects of variability in the progenitor. We have attempted to quantify some of these effects, and in particular we investigated the effects of variability in Section 4.3.2 and found no significant change in the preferred dust model. Moreover, we do not expect these effects to change the overall luminosity of the system given the sampling of the SED or the finding that the SN 2025pht progenitor system experienced a large magnitude of circumstellar extinction.

Nevertheless, future analyses can account for some of these uncertainties in dust properties within the constraints of physically motivated priors by fitting RSG SEDs with (i) a variable dust composition between pure graphitic, pure silicate, or some arbitrary mixture of the two; (ii) variable dust geometries following a range of radial profiles and inner and outer dust shell ratios; and (iii) time-variable fits restricted to narrow ranges in time as in Figure 5. While it is possible that, via some combination of the above, we could find a range of parameter space that favors dust compositions other than graphitic, our best-fitting models consistently favor the highly extinguished $\log(L/L_\odot) = 5.0$ graphitic dust model discussed above.

Existing and future JWST observations (as well as Nancy Grace Roman Space Telescope imaging; S. Gezari et al. 2022; L. Lancaster et al. 2022; K. C. Dage et al. 2023) will enable these more sophisticated dust fitting prescriptions even for the vast population of RSGs observed in situ for nearby galaxies such as NGC 1637. Indeed, the peculiar nature of the SN 2025pht progenitor, and in particular its highly reddened SED consistent with graphitic dust, may be an avenue for identifying RSGs in the final phases of evolution before explosion (i.e., "superwind" or post-outburst RSGs; V. Morozova et al. 2020; B. Davies et al. 2022). Along with follow-up of low-luminosity eruptive sources coincident with RSGs (similar to SN 2020tlf; W. V. Jacobson-Galán et al. 2022) and other highly variable RSGs (similar to

SN 2023ixf; C. D. Kilpatrick et al. 2023a; J. E. Jencson et al. 2023), surveying these mid-IR bright RSGs may be the most promising avenue toward obtaining spectral classification of an SN progenitor star in the final months or years before explosion. This would allow us to definitively answer questions about spectral type, stellar mass, metallicity, circumstellar extinction, dust composition, and the presence of a companion star in SN progenitor systems that are obscured via broadband SED fitting.

6. Conclusions

We present an analysis of the SN II SN 2025pht in NGC 1637 at 12 Mpc and the detection of its counterpart in pre-explosion JWST and HST imaging. From our analysis, we find the following:

1. The counterpart is detected at wavelengths from WFPC2/F814W ($\approx$0.8 μm) to MIRI/F770W (7.6 μm), representing one of the best-sampled SN progenitor candidates to date in wavelength, including the first detection of a counterpart at wavelengths >5 μm.
2. From these data, we fit dust-obscured RSG SEDs and find that the source is moderately luminous with $\log(L/L_{\odot}) = 5.0$ (corresponding to an initial mass of ≈ 15 $M_{\odot}$) but also heavily dust obscured. In our best-fitting model, we prefer graphite-rich dust with a high line-of-sight optical extinction of $A_V = 5.3$ mag.
3. The implied carbon-rich dust composition is unusual for high-mass RSGs that tend to be oxygen-rich and produce silicates in their circumstellar environments. If the SN 2025pht counterpart had a carbon-rich circumstellar environment, it may imply that the surface abundances of some evolved, carbon-burning and later RSGs are significantly enhanced owing to convection.
4. Along with SN 2017eaw, SN 2023ixf, and SN 2024ggi, SN 2025pht belongs to a class of sources with pre-explosion counterparts detected at >2 μm. These sources are all consistent with moderate to heavy circumstellar reddening in the underlying RSG, significantly in excess of previous predictions on the magnitude of circumstellar extinction for SN progenitor stars. New analyses of the overall population of SN II progenitor stars that incorporate these constraints on their typical circumstellar extinction may mitigate or entirely erase the mismatch between their luminosities and the overall populations of RSGs.

SN 2025pht represents the beginning of SN progenitor star analyses performed with JWST. As shown above, the broad wavelength coverage and precise photometry enabled by NIRCam and MIRI can enable novel constraints on the nature of the circumstellar environment around these sources and more precise estimates of their bolometric luminosities. By answering long-standing questions about the terminal states of massive stars, we are now better able to bridge the gap between direct imaging of SN progenitor systems and indirect constraints from their pre-explosion outbursts (W. V. Jacobson-Galán et al. 2022), early light curves (G. Hosseinzadeh et al. 2018, 2022; C. D. Kilpatrick et al. 2023b), and flash spectroscopy (W. V. Jacobson-Galán et al. 2024).

Acknowledgments

We would like to thank STScI scientists Amber Armstrong, Joel Green, and Christian Soto for supporting and triggering HST-GO-17706.

C.D.K. and A.S. gratefully acknowledge support from the NSF through AST-2432037, from the HST Guest Observer Program through HST-SNAP-17070 and HST-GO-17706, and from JWST Archival Research through JWST-AR-6241 and JWST-AR-5441. The UCSC team is supported in part by NASA grants 80NSSC23K0301 and 80NSSC24K1411, JWST Archival Research through JWST-AR-6241 and JWST-AR-5441, and a fellowship from the David and Lucile Packard Foundation to R.J.F. M.R.D acknowledges support from the NSERC through grant RGPIN-2019-06186, the Canada Research Chairs Program, and the Dunlap Institute at the University of Toronto. A.G. is supported by the National Science Foundation under Cooperative Agreement PHY-2019786 (The NSF AI Institute for Artificial Intelligence and Fundamental Interactions, http://iaifi.org/). W.V.J.-G. is supported by NASA through Hubble Fellowship grant HSTHF2-51558.001-A awarded by the Space Telescope Science Institute, which is operated for NASA by the Association of Universities for Research in Astronomy, Inc., under contract NAS5-26555.

This research is based on observations made with the NASA/ESA Hubble Space Telescope obtained from the Space Telescope Science Institute, which is operated by the Association of Universities for Research in Astronomy, Inc., under NASA contract NAS 5–26555. These observations are associated with programs HST-GO-5446 (PI Illingworth), HST-GO-9041 (PI Smartt), HST-SNAP-9042 (PI Smartt), HST-GO-9155 (PI Leonard), HST-GO-17502 (PI Thilker), and HST-GO-17706 (PI Kilpatrick).

This work is based in part on observations made with the NASA/ESA/CSA James Webb Space Telescope. The data were obtained from the Mikulski Archive for Space Telescopes at the Space Telescope Science Institute, which is operated by the Association of Universities for Research in Astronomy, Inc., under NASA contract NAS 5-03127 for JWST. These observations are associated with programs JWST-GO-3707 (PI Leroy) and JWST-GO-4793 (PI Shinnerer).

Some of the data presented herein were obtained at Keck Observatory, which is a private 501(c)3 nonprofit organization operated as a scientific partnership among the California Institute of Technology, the University of California, and the National Aeronautics and Space Administration. The Observatory was made possible by the generous financial support of the W. M. Keck Foundation.

The authors wish to recognize and acknowledge the very significant cultural role and reverence that the summit of Maunakea has always had within the Native Hawaiian community. We are most fortunate to have the opportunity to conduct observations from this mountain.

Facilities: HST (WFPC2, WFC3), JWST (NIRCam, MIRI), Keck:I (LRIS).

Software: `astropy` (Astropy Collaboration et al. 2013, 2018, 2022), `dolphot` (A. Dolphin 2016), `drizzlepac` (W. J. Hack et al. 2021), `dusty` (Z. Ivezic & M. Elitzur 1997), `emcee` (D. Foreman-Mackey et al. 2013), `extinction` (K. Gordon 2024), `hst123` (C. D. Kilpatrick 2021), `JHAT` (A. Rest et al. 2023), `SNID` (S. Blondin &

J. L. Tonry 2011), `synphot` (P. Lian Lim 2020), `TweakReg` (R. A. Lucas & B. Hilbert 2015), `UCSC Spectral Pipeline` (M. R. Siebert et al. 2020), `progenitors` (C. D. Kilpatrick 2025).

Data and Software Availability

All data and analysis products presented in this article are available upon request. Analysis code and photometry used in this Letter are available on GitHub;[16] a copy of version 1.1.0 has been deposited to Zenodo: doi:10.5281/zenodo.17082142 (C. D. Kilpatrick 2025). The Hubble Space Telescope and James Webb Space Telescope data used in this Letter can be found in MAST: doi:10.17909/dj00-e351.

ORCID iDs

Charles D. Kilpatrick https://orcid.org/0000-0002-5740-7747
Aswin Suresh https://orcid.org/0009-0005-8230-030X
Kyle W. Davis https://orcid.org/0000-0002-5680-4660
Maria R. Drout https://orcid.org/0000-0001-7081-0082
Ryan J. Foley https://orcid.org/0000-0002-2445-5275
Alexander Gagliano https://orcid.org/0000-0003-4906-8447
Wynn V. Jacobson-Galán https://orcid.org/0000-0002-3934-2644
Ravjit Kaur https://orcid.org/0009-0005-1871-7856
Kirsty Taggart https://orcid.org/0000-0002-5748-4558
Jason Vazquez https://orcid.org/0000-0003-1576-0830

References

Adams, S. M., Kochanek, C. S., Gerke, J. R., Stanek, K. Z., & Dai, X. 2017, MNRAS, 468, 4968
Arnett, W. D., Bahcall, J. N., Kirshner, R. P., & Woosley, S. E. 1989, ARA&A, 27, 629
Astropy Collaboration, Price-Whelan, A. M., Lim, P. L., et al. 2022, ApJ, 935, 167
Astropy Collaboration, Price-Whelan, A. M., Sipőcz, B. M., et al. 2018, AJ, 156, 123
Astropy Collaboration, Robitaille, T. P., Tollerud, E. J., et al. 2013, A&A, 558, A33
Beasor, E. R., Smith, N., & Jencson, J. E. 2025, ApJ, 979, 117
Blanchard, P. K., Berger, E., Andrew, S. E., et al. 2025, ApJL, 989, L49
Blondin, S., & Tonry, J. L., 2011 SNID: Supernova Identification, Astrophysics Source Code Library, ascl:1107.001
Bruch, R. J., Gal-Yam, A., Schulze, S., et al. 2021, ApJ, 912, 46
Bushouse, H., Eisenhamer, J., Dencheva, N., et al. 2023, JWST Calibration Pipeline, v1.12.5, Zenodo, doi:10.5281/zenodo.10022973
Byrne, R. A., & Fraser, M. 2022, MNRAS, 514, 1188
Choi, J., Dotter, A., Conroy, C., et al. 2016, ApJ, 823, 102
Conroy, C., Strader, J., van Dokkum, P., et al. 2018, ApJ, 864, 111
Dage, K. C., Usher, C., Sobeck, J., et al. 2023, arXiv:2306.12620
Davies, B., & Beasor, E. R. 2018, MNRAS, 474, 2116
Davies, B., & Beasor, E. R. 2020a, MNRAS, 493, 468
Davies, B., & Beasor, E. R. 2020b, MNRAS, 496, L142
Davies, B., & Dessart, L. 2019, MNRAS, 483, 887
Davies, B., Figer, D. F., Kudritzki, R.-P., et al. 2007, ApJ, 671, 781
Davies, B., Kudritzki, R.-P., Plez, B., et al. 2013, ApJ, 767, 3
Davies, B., & Plez, B. 2021, MNRAS, 508, 5757
Davies, B., Plez, B., & Petrault, M. 2022, MNRAS, 517, 1483
De, K., MacLeod, M., Jencson, J. E., et al. 2024, arXiv:2410.14778
De Beck, E., Andrews, H., Quintana-Lacaci, G., & Vlemmings, W. H. T. 2025, A&A, 698, A179
de Wit, S., Bonanos, A. Z., Antoniadis, K., et al. 2024, A&A, 689, A46
Dessart, L. 2025, A&A, 694, A132
Dessart, L., & Jacobson-Galán, W. V. 2023, A&A, 677, A105
Dolphin, A., 2023 DOLPHOT: Stellar Photometry, Astrophysics Source Code Library, ascl:1608.013
Draine, B. T., & Lee, H. M. 1984, ApJ, 285, 89
Ekström, S., Georgy, C., Eggenberger, P., et al. 2012, A&A, 537, A146
Eldridge, J. J., & Tout, C. A. 2004, MNRAS, 353, 87
Ertl, T., Janka, H. T., Woosley, S. E., Sukhbold, T., & Ugliano, M. 2016, ApJ, 818, 124
Farrell, E. J., Groh, J. H., Meynet, G., & Eldridge, J. J. 2020, MNRAS, 494, L53
Fernández, R., Quataert, E., Kashiyama, K., & Coughlin, E. R. 2018, MNRAS, 476, 2366
Fitzpatrick, E. L. 1999, PASP, 111, 63
Foley, R. J., Papenkova, M. S., Swift, B. J., et al. 2003, PASP, 115, 1220
Foreman-Mackey, D., Hogg, D. W., Lang, D., & Goodman, J. 2013, PASP, 125, 306
Förster, F., Moriya, T. J., Maureira, J. C., et al. 2018, NatAs, 2, 808
Fraser, M., Maund, J. R., Smartt, S. J., et al. 2014, MNRAS, 439, L56
Fuller, J., & Tsuna, D. 2024, OJAp, 7, 47
Gal-Yam, A., Arcavi, I., Ofek, E. O., et al. 2014, Natur, 509, 471
Galbany, L., Hamuy, M., Phillips, M. M., et al. 2016a, AJ, 151, 33
Galbany, L., Stanishev, V., Mourão, A. M., et al. 2016b, A&A, 591, A48
Gezari, S., Bentz, M., De, K., et al. 2022, arXiv:2202.12311
Gordon, K. 2024, JOSS, 9, 7023
Gustafsson, B., Edvardsson, B., Eriksson, K., et al. 2008, A&A, 486, 951
Hack, W. J., Cara, M., Sosey, M., et al. 2021, spacetelescope/drizzlepac: Drizzlepac v3.3.0, Zenodo, doi:10.5281/zenodo.5534751
Healy, S., Horiuchi, S., & Ashall, C. 2024, arXiv:2412.04386
Horne, K. 1986, PASP, 98, 609
Hosseinzadeh, G., Kilpatrick, C. D., Dong, Y., et al. 2022, ApJ, 935, 31
Hosseinzadeh, G., Valenti, S., McCully, C., et al. 2018, ApJ, 861, 63
Ivezic, Z., & Elitzur, M. 1997, MNRAS, 287, 799
Jacobson-Galán, W. V., Dessart, L., Davis, K. W., et al. 2024, ApJ, 970, 189
Jacobson-Galán, W. V., Dessart, L., Jones, D. O., et al. 2022, ApJ, 924, 15
Jacobson-Galán, W. V., Dessart, L., Margutti, R., et al. 2023, ApJL, 954, L42
Jencson, J. E., Pearson, J., Beasor, E. R., et al. 2023, ApJL, 952, L30
Khazov, D., Yaron, O., Gal-Yam, A., et al. 2016, ApJ, 818, 3
Kilpatrick, C. D. 2021, charliekilpatrick/hst123: hst123, v1.0.0, Zenodo, doi:10.5281/zenodo.5573941
Kilpatrick, C. D. 2025, charliekilpatrick/progenitors: Release for Kilpatrick et al. 2025 on SN 2025pht, v1.1.0, Zenodo, doi:10.5281/zenodo.17082142
Kilpatrick, C. D., & Foley, R. J. 2018, MNRAS, 481, 2536
Kilpatrick, C. D., Foley, R. J., Jacobson-Galán, W. V., et al. 2023a, ApJL, 952, L23
Kilpatrick, C. D., Izzo, L., Bentley, R. O., et al. 2023b, MNRAS, 524, 2161
Kirshner, R. P., Sonneborn, G., Crenshaw, D. M., & Nassiopoulos, G. E. 1987, ApJ, 320, 602
Kochanek, C. S. 2014, ApJ, 785, 28
Kochanek, C. S. 2020, MNRAS, 493, 4945
Kochanek, C. S., Khan, R., & Dai, X. 2012, ApJ, 759, 20
Kochanek, C. S., Shappee, B. J., Stanek, K. Z., et al. 2017, PASP, 129, 104502
Lancaster, L., Pearson, S., Williams, B. F., et al. 2022, AJ, 164, 142
Lançon, A., Hauschildt, P. H., Ladjal, D., & Mouhcine, M. 2007, A&A, 468, 205
Li, W., Van Dyk, S. D., Filippenko, A. V., et al. 2006, ApJ, 641, 1060
Lian Lim, P. 2020, synphot, v1.0.1, Zenodo, doi:10.5281/zenodo.3971036
Limongi, M., Roberti, L., Chieffi, A., & Nomoto, K. 2024, ApJS, 270, 29
Lucas, R. A., & Hilbert, B. 2015, Basic Use of SExtractor Catalogs With TweakR eg - I, Instrument Science Report ACS 2015-04,
Maeder, A., & Meynet, G. 2000, A&A, 361, 159
Martinez, L., Anderson, J. P., Bersten, M. C., et al. 2022, A&A, 660, A42
Mathis, J. S., Rumpl, W., & Nordsieck, K. H. 1977, ApJ, 217, 425
Maund, J. R., Fraser, M., Smartt, S. J., et al. 2013, MNRAS, 431, L102
Morozova, V., Piro, A. L., Fuller, J., & Van Dyk, S. D. 2020, ApJL, 891, L32
Morozova, V., Piro, A. L., & Valenti, S. 2018, ApJ, 858, 15
Neustadt, J. M. M., Kochanek, C. S., & Smith, M. R. 2024, MNRAS, 527, 5366
Niu, Z., Sun, N.-C., Maund, J. R., et al. 2023, ApJL, 955, L15
O'Connor, E., & Ott, C. D. 2011, ApJ, 730, 70
Oke, J. B., Cohen, J. G., Carr, M., et al. 1995, PASP, 107, 375
Oke, J. B., & Gunn, J. E. 1983, ApJ, 266, 713
O'Neill, D., Kotak, R., Fraser, M., et al. 2019, A&A, 622, L1
Phillips, M. M., Simon, J. D., Morrell, N., et al. 2013, ApJ, 779, 38
Piro, A. L. 2013, ApJL, 768, L14
Pledger, J. L., & Shara, M. M. 2023, ApJL, 953, L14
Poznanski, D., Prochaska, J. X., & Bloom, J. S. 2012, MNRAS, 426, 1465

[16] https://github.com/charliekilpatrick/progenitors

Rest, A., Pierel, J., Correnti, M., et al. 2023, arminrest/jhat: The JWST HST Alignment Tool (JHAT), v2, Zenodo, doi:10.5281/zenodo.7892935
Saha, A., Thim, F., Tammann, G. A., Reindl, B., & Sandage, A. 2006, ApJS, 165, 108
Sahu, D. K., Anupama, G. C., Srividya, S., & Muneer, S. 2006, MNRAS, 372, 1315
Savage, B. D., & Mathis, J. S. 1979, ARA&A, 17, 73
Schlafly, E. F., & Finkbeiner, D. P. 2011, ApJ, 737, 103
Shappee, B. J., Prieto, J. L., Grupe, D., et al. 2014, ApJ, 788, 48
Siebert, M. R., Dimitriadis, G., Polin, A., & Foley, R. J. 2020, ApJL, 900, L27
Silverman, J. M., Foley, R. J., Filippenko, A. V., et al. 2012, MNRAS, 425, 1789
Smartt, S. J. 2009, ARA&A, 47, 63
Smartt, S. J. 2015, PASA, 32, e016
Smith, N., Li, W., Filippenko, A. V., & Chornock, R. 2011, MNRAS, 412, 1522
Sollerman, J., Yang, S., Schulze, S., et al. 2021, A&A, 655, A105
Soraisam, M. D., Bildsten, L., Drout, M. R., et al. 2018, ApJ, 859, 73
Soraisam, M. D., Szalai, T., Van Dyk, S. D., et al. 2023, ApJ, 957, 64
Springob, C. M., Haynes, M. P., Giovanelli, R., & Kent, B. R. 2005, ApJS, 160, 149
Stanek, K. Z., & Petz, S. 2025, TNSTR, 2025-2463, 1
Stritzinger, M. D., Anderson, J. P., Contreras, C., et al. 2018, A&A, 609, A134
Sugimoto, D., & Nomoto, K. 1980, SSRv, 25, 155
Sukhbold, T., Ertl, T., Woosley, S. E., Brown, J. M., & Janka, H.-T. 2016, ApJ, 821, 38
Taniguchi, D., Yamazaki, K., & Uno, S. 2022, NatAs, 6, 930
Teja, R. S., Singh, A., Sahu, D. K., et al. 2022, ApJ, 930, 34
Tomasella, L., Cappellaro, E., Fraser, M., et al. 2013, MNRAS, 434, 1636
Van Dyk, S. D. 2017, RSPTA, 375, 20160277
Van Dyk, S. D., Bostroem, K. A., Zheng, W., et al. 2023a, MNRAS, 524, 2186
Van Dyk, S. D., Cenko, S. B., Poznanski, D., et al. 2012, ApJ, 756, 131
Van Dyk, S. D., de Graw, A., Baer-Way, R., et al. 2023b, MNRAS, 519, 471
Van Dyk, S. D., Srinivasan, S., Andrews, J. E., et al. 2024, ApJ, 968, 27
Van Dyk, S. D., Zheng, W., Brink, T. G., et al. 2018, ApJ, 860, 90
van Loon, J. T. 2025, Galax, 13, 72
van Loon, J. T., Cioni, M. R. L., Zijlstra, A. A., & Loup, C. 2005, A&A, 438, 273
Verhoelst, T., van der Zypen, N., Hony, S., et al. 2009, A&A, 498, 127
Walmswell, J. J., & Eldridge, J. J. 2012, MNRAS, 419, 2054
Wang, T., Jiang, B., Ren, Y., Yang, M., & Li, J. 2021, ApJ, 912, 112
West, R. M., Lauberts, A., Jorgensen, H. E., & Schuster, H. E. 1987, A&A, 177, L1
Woosley, S. E., Pinto, P. A., Martin, P. G., & Weaver, T. A. 1987, ApJ, 318, 664
Xiang, D., Mo, J., Wang, X., et al. 2024, ApJL, 969, L15
Yaron, O., & Gal-Yam, A. 2012, PASP, 124, 668
Zapartas, E., de Mink, S. E., Justham, S., et al. 2021, A&A, 645, A6